Exploring space separation techniques for 3D elastic waves simulations

Dimitri Goutaudier[1] · **Laurent Berthe**[1] · **Francisco Chinesta**[2]

Abstract
This paper explores numerical methods dedicated to 3D elastic waves simulations in spatially separable domains such as plates. The objective is to reduce the computation time and the memory requirements associated to these large simulations involving fine space and time discretizations. The 3D problem is decomposed into a sequence of lower dimensional problems with the Proper Generalized Decomposition. The spatial discretization is performed with the Spectral Element Method to provide more compact separated representations compared to the ones obtained with a finite element discretization. Following previous works on space separation in elastodynamics, we explore hybrid explicit/implicit time marching schemes to improve the solution through one direction as needed, without decreasing the time step due to stability constraints. Large 3D numerical problems with several millions of degrees of freedom are efficiently solved with memory requirements characteristic of 2D problems.

Keywords Elastodynamics · Elastic waves · Proper generalized decomposition (PGD) · Spectral element method (SEM) · Hybrid time integration · Composite laminate

1 Introduction

The accurate description of wave propagation phenomena is important in many applications. Laser shock adhesion tests, for instance, consist in applying intense pressures, highly concentrated both in space and in time, on two opposite faces of a laminate target [1–3]. This latter consists in a stacking of Carbon Fiber Reinforced Polymer (CFRP) plies with different orientations, bonded together with epoxy resin. The scattered propagation of elastic waves in such a layered medium is complex, and numerical simulations are necessary to understand experimental measurements embedding many phenomena (material behavior, scattering patterns, edge effects etc.).

Unfortunately, significant numerical difficulties arise when it comes to solve a wave propagation problem. First, an important computational effort is required with three-dimensional spatial domains. A fine spatial discretization is indeed necessary to capture excited waves with small wavelength (spatial resolution), and a fine time discretization must be used to observe high speed propagation (time resolution). These requirements easily lead to costly simulations, especially if the applied loading has very short duration (the frequency content is broader hence excited wavelengths are smaller), for instance when addressing laser shocks. Second, standard solvers based on the finite element method exhibit poor dispersion properties [4]. Numerical solutions computed with the finite element method may be polluted with spurious high frequency oscillations [5,6]. These latter are then hard to distinguish from physical waves when the medium is complex, especially in layered media that scatter the wave field at each interface crossing [7]. To circumvent this limitation, specific time marching schemes can be used to introduce numerical dissipation with tunable parameters [8,9]. Other numerical methods can be used to solve wave propagation problems with reduced dispersion, such as boundary integral methods [10,11], space-time finite element methods [12,13], or the spectral element method [14–17].

As mentioned above, numerous numerical methods solve wave propagation problems with controlled accuracy and good convergence properties. Yet, even if the spatial domain

✉ Dimitri Goutaudier
dimitri.goutaudier@gmail.com

[1] PIMM, CNRS, HESAM, CNAM, Arts et Métiers Institute of Technology, 151 boulevard de l'Hôpital, 75013 Paris, France

[2] ESI GROUP Chair @ PIMM, Arts et Métiers Institute of Technology, Paris, France

is as simple as a plate, the computational effort remains prohibitive if appropriate numerical resources are not available. Different approaches have been developed to tackle large-scale simulations with parallel computing strategies [18–20]. For instance, Zhang et al. presented in [20] a parallel explicit solver based on the scaled boundary finite element method, with an efficient pre-computation approach and element-wise operations.

In practice, it is common situation that restriction accesses to intensive calculation centres slow down the research efforts. It is then difficult to use efficient solvers performing massively parallel calculations. The objective of the present work is to provide a numerical method dedicated to 3D wave propagation problems, compatible with standard computing and programming platforms generally available in research teams. The main limitation of the presented method is the restriction to simple spatial domains with at least one extrusion direction (e.g. plate, cylinder). This paper is a continuation of our previous work [21] validated on two-dimensional configurations.

This paper is organized as follows. In Sect. 2, we recall the variational formulation of the three-dimensional elastic waves equation and its time discretization. Then we present our proposal to reduce the computational effort. The three-dimensional spatial domain is decomposed into a sequence of lower dimension problems with the Proper Generalized Decomposition [22]. The spectral element method is implemented in this space separation framework to improve the accuracy and reduce numerical dispersion compared to the finite element method. An original time marching scheme, originally introduced in [23], is presented to improve the solution through one direction as needed, without decreasing the time step and affecting the computation time. In this framework, the spectral element method enables a true hybrid explicit/implicit scheme with promising behavior on the computation time. Section 3 is devoted to numerical experiments with space separation techniques. The convergence properties are first discussed on a simple two-dimensional example. Then three-dimensional test cases, in isotropic and anisotropic elastic media, are considered to evaluate the numerical performances of the proposed approach. Simulations are carried out with a standard programming software (Matlab) on a laptop to evidence the reduction of the computation time and the memory needs.

2 Space separation of 3D elastic waves equations

We consider an elastic inhomogeneous medium occupying a spatially separable domain $\Omega \subset \mathbb{R}^3$, namely either of the form $\Omega = \Omega_{xy} \times \Omega_z$ (plate, cylinder etc.) or $\Omega = \Omega_x \times \Omega_y \times \Omega_z$ (hexahedral domain). Space separation methods are therefore limited to domains with an extrusion direction, although domains with appropriate geometrical properties can be considered [24].

2.1 Governing equations

We adopt in this paper the notations employed in [15]. The displacement vector at a point $\mathbf{x} \in \Omega$ at time $t \in I = [0, T]$ is denoted by $\mathbf{u}(\mathbf{x}, t)$, where I is the time interval of interest. The velocity and acceleration fields are denoted by $\dot{\mathbf{u}}$ and $\ddot{\mathbf{u}}$, respectively. We consider the equations of elastic wave propagation given by:

$$\rho \ddot{\mathbf{u}} = \mathrm{div}[\boldsymbol{\sigma}] + \mathbf{f} \tag{1}$$

with the initial conditions:

$$\mathbf{u}(\mathbf{x}, 0) = \mathbf{u}_0(\mathbf{x}) \tag{2}$$

$$\dot{\mathbf{u}}(\mathbf{x}, 0) = \mathbf{v}_0(\mathbf{x}) \tag{3}$$

where $\rho(\mathbf{x})$ is the mass density, $\boldsymbol{\sigma}(\mathbf{x}, t)$ is the stress tensor, $\mathbf{f}(\mathbf{x}, t)$ is the body force, $\mathbf{u}_0(\mathbf{x})$ and $\mathbf{v}_0(\mathbf{x})$ are the initial displacement and velocity fields, respectively. The stress tensor is determined by Hooke's law:

$$\boldsymbol{\sigma} = \mathbf{C} : \boldsymbol{\epsilon} \tag{4}$$

where $\mathbf{C}(\mathbf{x})$ is the fourth order elastic tensor and where the strain tensor $\boldsymbol{\epsilon}$ is given by:

$$\boldsymbol{\epsilon} = \nabla_s \mathbf{u} = \frac{1}{2}\left[\nabla \mathbf{u} + (\nabla \mathbf{u})^T\right] \tag{5}$$

In components form, the stress-strain relation is then $\sigma_{ij}(\mathbf{x}, t) = C_{ijkl}(\mathbf{x})\epsilon_{k,l}(\mathbf{x}, t)$.

The boundary of Ω is decomposed into three distinct portions Γ_N, Γ_D and Γ_{abs} where we impose, respectively, tractions, displacements and fictitious tractions to absorb incident waves:

$$\boldsymbol{\sigma}(\mathbf{x}, t) \cdot \mathbf{n}(\mathbf{x}, t) = \mathbf{t}(\mathbf{x}, t) \qquad \text{on } \Gamma_N \tag{6}$$

$$\mathbf{u}(\mathbf{x}, t) = \mathbf{g}(\mathbf{x}, t) \qquad \text{on } \Gamma_D \tag{7}$$

$$\boldsymbol{\sigma}(\mathbf{x}, t) \cdot \mathbf{n}(\mathbf{x}, t) = \boldsymbol{\tau}(\mathbf{x}, t) \qquad \text{on } \Gamma_{\text{abs}} \tag{8}$$

where $\mathbf{n}$ is the unit outward normal to the surface, $\mathbf{t}(\mathbf{x}, t)$ is the prescribed boundary traction vector, $\mathbf{g}(\mathbf{x}, t)$ is the prescribed displacement field, and $\boldsymbol{\tau}(\mathbf{x}, t)$ is the absorbing boundary traction. In this study, we use the absorbing boundary conditions (ABCs) based on a paraxial approximation of the elastic waves equation introduced in [25]. These ABCs, denoted P-ABCs in the following, are exact for incident waves normal to the surface and less accurate as the angle

$$\boldsymbol{\tau} = \rho c_n \left[\dot{\mathbf{u}} \cdot \mathbf{n}\right] \cdot \mathbf{n} + \rho c_{t_1} \left[\dot{\mathbf{u}} \cdot \mathbf{t}_1\right] \cdot \mathbf{t}_1 + \rho c_{t_2} \left[\dot{\mathbf{u}} \cdot \mathbf{t}_2\right] \cdot \mathbf{t}_2 \quad (9)$$

where c_n is the velocity of P-waves (longitudinal) propagating in the direction of the normal $\mathbf{n}$ of the surface, c_{t_1} and c_{t_2} are velocities of S-waves (transverse) also propagating in direction $\mathbf{n}$, but with polarizations along unit orthogonal vectors $\mathbf{t}_1$ and $\mathbf{t}_2$ tangential to the surface, respectively. This P-ABC is therefore limited to orthotropic materials whose principal axes are aligned with the normal and tangential directions of the surface boundaries, otherwise such P- and S-waves would not exist [26].

More efficient ABCs could be implemented within a space separation framework, such as Perfectly Matched Layers (PML, [27]) or Absorbing Layers using Increasing Damping (ALID, [28]), but they would increase the computational effort. The purpose of this study is not to minimize spurious reflections, but to resort to space separation techniques to significantly reduce the computation time while preserving a satisfactory accuracy. In addition, stability issues should be addressed with more advanced ABCs. PMLs are indeed very effective with isotropic elastic materials but are unstable in general with orthotropic materials [29]. ALID should be used in this case, and asynchronous strategies could be considered in future works to alleviate the computational cost by using a larger time step in the ALID domain [30].

2.2 Variational formulation

The solution $\mathbf{u}$ is searched in the space of kinematically admissible displacements:

$$\mathcal{U}_t = \{\mathbf{u}(\mathbf{x}, t) \in H^1(\Omega); \mathbf{u}(\mathbf{x}, t) = \mathbf{g}(\mathbf{x}, t) \text{ on } \Gamma_D \times I\} \quad (10)$$

and a function space of test functions $\mathbf{u}^*$ is introduced:

$$\mathcal{V} = \{\mathbf{u}^*(\mathbf{x}) \in H^1(\Omega); \mathbf{u}^*(\mathbf{x}) = \mathbf{0} \text{ on } \Gamma_D\} \quad (11)$$

The variational formulation of the elastodynamic problem (1-8) then reads: find $\mathbf{u} \in \mathcal{U}_t$, such that for any $t \in I$ and any $\mathbf{u}^* \in \mathcal{V}$:

$$\begin{aligned} &\int_\Omega \rho \mathbf{u}^* \cdot \ddot{\mathbf{u}} dV + \int_\Omega \nabla_s \mathbf{u}^* : \mathbf{C} : \nabla_s \mathbf{u} dV \\ &= \int_\Omega \mathbf{u}^* \cdot \mathbf{f} dV + \int_{\Gamma_N} \mathbf{u}^* \cdot \mathbf{t} d\Gamma + \int_{\Gamma_{\text{abs}}} \mathbf{u}^* \cdot \boldsymbol{\tau} d\Gamma \end{aligned} \quad (12)$$

with:

$$\int_\Omega \mathbf{u}^* \cdot \mathbf{u}(\mathbf{x}, 0) dV = \int_\Omega \mathbf{u}^* \cdot \mathbf{u}_0(\mathbf{x}) dV \quad (13)$$

$$\int_\Omega \mathbf{u}^* \cdot \dot{\mathbf{u}}(\mathbf{x}, 0) dV = \int_\Omega \mathbf{u}^* \cdot \mathbf{v}_0(\mathbf{x}) dV \quad (14)$$

2.3 Discretization in time

We discretize the time interval of interest with a constant time step Δt. The time increments are then denoted by $t_k = k\Delta t$. We use a hybrid time integration scheme (see Sect. 2.7) inspired from the widely employed Newmark schemes based on the following approximations [31]:

$$\dot{\mathbf{u}}^{k+1} \approx \dot{\mathbf{u}}^k + \frac{\Delta t}{2}(\ddot{\mathbf{u}}^k + \ddot{\mathbf{u}}^{k+1}) \quad (15)$$

$$\mathbf{u}^{k+1} \approx \mathbf{u}^k + \Delta t \dot{\mathbf{u}}^k + \frac{\Delta t^2}{2}\left[(1-2\alpha)\ddot{\mathbf{u}}^k + \alpha \ddot{\mathbf{u}}^{k+1}\right] \quad (16)$$

where the superscript $(.)^k$ refers to an evaluation at time t_k. These relations lead to unconditionally stable schemes if, and only if, $\alpha \geq 1/4$. For instance, $\alpha = 0$ is the central difference method (explicit, conditionally stable) and $\alpha = 1/4$ is the trapezoidal rule (implicit, unconditionally stable). The variational formulation is discretized in time by using the above relations with a linear combination of equation (12) evaluated at times t_{k-1}, t_k and t_{k+1}. Given the solution known at times t_{k-1} and t_k, the problem is now to find the solution at time t_{k+1} satisfying the following relation:

$$\begin{aligned} &\int_\Omega \rho \mathbf{u}^* \cdot \frac{\mathbf{u}^{k+1} - 2\mathbf{u}^k + \mathbf{u}^{k-1}}{\Delta t^2} dV + \int_\Omega \nabla_s \mathbf{u}^* : \mathbf{C} : \nabla_s \mathbf{u}^\alpha dV \\ &= \int_\Omega \mathbf{u}^* \cdot \mathbf{f}^\alpha dV + \int_{\Gamma_N} \mathbf{u}^* \cdot \mathbf{t}^\alpha d\Gamma \\ &\quad + \int_{\Gamma_{\text{abs}}} \mathbf{u}^* \cdot \boldsymbol{\tau}^\alpha d\Gamma \end{aligned} \quad (17)$$

where we adopted the notation $(.)^\alpha = \alpha(.)^{k+1} + (1-2\alpha)(.)^k + \alpha(.)^{k-1}$ for the sake of clarity. More advanced time marching schemes could be considered to control numerical dissipation and dispersion [9].

2.4 Time adaptive space separation

Separation of variables consists in approximating the solution under separated form to break down a high dimensional problem into a sequence of problems of lower dimension, much cheaper to be solved. In 3D statics, there is no other possibility than performing an in-plane/out-of-plane space separation, or a full space separation, by approximating the solution with one of the following relations [32], respectively:

$$u_i(x, y, z) \approx \sum_{j=1}^{M} \phi_{ij}(x, y) \psi_{ij}(z) \quad (18)$$

$$u_i(x,y,z) \approx \sum_{j=1}^{M} \phi_{ij}(x)\chi_{ij}(y)\psi_{ij}(z) \tag{19}$$

where u_i denotes a component of the 3D displacement field $\mathbf{u} = (u_1, u_2, u_3)$. Such a separated form is built up on the fly, directly from the variational formulation of the problem, with a Proper Generalized Decomposition (PGD) solver [22].

In elastodynamics, however, the time variable must be taken into account and several alternatives can be considered. In low and medium frequency domains, the space-time separation has been successfully validated with standard PGD techniques [33,34]. It consists in introducing separated functions depending on the time variable in (18) or (19). Regarding wave propagation problems, however, convergence difficulties have been reported with the space-time separation ($M \gg 100$). Boucinha et al. [35,36] circumvented this issue by developing a PGD solver based on a Time Discontinuous Galerkin framework with a compression strategy to enforce a low-rank approximation of the solution. Yet, even if their method achieves important memory gains, the computation time is as high as the one obtained with standard solvers without separation of variables.

As an alternative, Quaranta et al. [23] proposed performing a space separation, either with (18) or (19), at each time step to compute a space separated form of the solution within a PGD-based time incremental solver. In our previous work [21], we evidenced that this time incremental procedure is in fact well adapted to wave propagation problems. Indeed, the propagation of a planar wave is mathematically described with a phase variable of the form $\mathbf{k}\cdot\mathbf{x} - \omega t$, with ω the wave frequency and $\mathbf{k}$ the propagation vector [37]. It informs that space and time variables are linked to efficiently describe the propagative behavior of the solution. In addition, we emphasized that an adaptive number of terms shall be introduced to get a wave propagation friendly separated form of the solution. The number of terms is then capable of evolving through time as needed, depending on the applied loading and the expansion of the waves in the medium. In particular, we showed that the number of terms stabilizes when the waves reach the boundaries of the domain. As a continuation of this work, validated on 2D test cases only, we consider herein the following time adaptive separated forms:

$$u_i(x,y,z,t_k) \approx \sum_{j=1}^{M_k} \phi_{ij}(x,y,t_k)\psi_{ij}(z,t_k) \tag{20}$$

$$u_i(x,y,z,t_k) \approx \sum_{j=1}^{M_k} \phi_{ij}(x,t_k)\chi_{ij}(y,t_k)\psi_{ij}(z,t_k) \tag{21}$$

In contrast to the work of Quaranta et al., we use efficient pre-operators in the PGD solver (Sect. 2.5), we resort to spectral elements instead of finite elements (Sect. 2.6), and we introduce a parameter in the hybrid explicit/implicit time marching scheme (Sect. 2.7).

2.5 Enrichment procedure with the proper generalized decomposition

In standard solvers, the unknowns of the 3D problem are the nodal values of the three components of the displacement field. A seemingly simple discretization grid with 100 nodes in each direction results in 10^6 unknowns at each time step (for each component of the displacement field), which already is a challenging numerical problem. In the proposed framework, however, the unknowns are the nodal values of the 2D or 1D functions involved in the separated representations (20) or (21). This problem is solved with a PGD algorithm as described in the following.

For generality, we present herunder the mathematical developments with the full space separation. The developments for the in-plane/out-of-plane separation can easily be deduced. Let $\mathbf{P}$, $\mathbf{Q}$ and $\mathbf{R}$ be vectors gathering shape functions associated to each spatial direction. The choice for the shape functions will be discussed in next section. Then we employ a nodal approximation:

$$\phi_{ij}(x,t_k) \approx \mathbf{P}(x)\cdot\boldsymbol{\Phi}_{ij}^k \tag{22}$$

$$\chi_{ij}(y,t_k) \approx \mathbf{Q}(y)\cdot\boldsymbol{X}_{ij}^k \tag{23}$$

$$\psi_{ij}(z,t_k) \approx \mathbf{R}(z)\cdot\boldsymbol{\Psi}_{ij}^k \tag{24}$$

where $\boldsymbol{\Phi}_{ij}^k$, $\boldsymbol{X}_{ij}^k$ and $\boldsymbol{\Psi}_{ij}^k$ denote the vectors of the nodal values of ϕ_{ij}, χ_{ij} and ψ_{ij} at time t_k, respectively.

The PGD solver computes the separated form with an enrichment procedure at each time step, by adding new terms to the solution at time t_{k+1} until a convergence criterion is satisfied. Assuming the first $n-1$ terms of (21) are known, the solution is enriched with a new term:

$$u_{i,n}^{k+1} = u_{i,n-1}^{k+1} + \phi_{in}\chi_{in}\psi_{in} \tag{25}$$

where the superscript $(.)^{k+1}$ is omitted on ϕ_{in}, χ_{in} and ψ_{in} for the sake of clarity. With the nodal approximation, the unknowns are the following vectors of nodal values:

$$\boldsymbol{\Phi}_n = (\boldsymbol{\Phi}_{1n}, \boldsymbol{\Phi}_{2n}, \boldsymbol{\Phi}_{3n}) \tag{26}$$

$$\boldsymbol{X}_n = (\boldsymbol{X}_{1n}, \boldsymbol{X}_{2n}, \boldsymbol{X}_{3n}) \tag{27}$$

$$\boldsymbol{\Psi}_n = (\boldsymbol{\Psi}_{1n}, \boldsymbol{\Psi}_{2n}, \boldsymbol{\Psi}_{3n}) \tag{28}$$

The enriched solution must satisfy the weak formulation discretized in time (17), which results in a nonlinear problem. The unknowns $\boldsymbol{\Phi}_n$, $\boldsymbol{X}_n$ and $\boldsymbol{\Psi}_n$ are computed with a fixed point method as follows. First, the nodal values of the

functions χ_{in} and ψ_{in} are assumed known, and the components of the arbitrary test field are taken under the form $u_i^* = \phi_{in}^* \chi_{in} \psi_{in}$. Upon substituting (22-25) in (17), and by assuming separated forms of all the fields, we find the following linear system to be solved (see Appendix):

$$\left[\sum_{i=1}^{n_A} \boldsymbol{A}_{1i}(\boldsymbol{X}_n^T \boldsymbol{A}_{2i} \boldsymbol{X}_n)(\boldsymbol{\Psi}_n^T \boldsymbol{A}_{3i} \boldsymbol{\Psi}_n)\right] \boldsymbol{\Phi}_n = \sum_{i=1}^{n_B} \boldsymbol{B}_{1i}[\boldsymbol{B}_{2i}^T \boldsymbol{X}_n \circ \boldsymbol{B}_{3i}^T \boldsymbol{\Psi}_n] \tag{29}$$

where $\circ$ denotes the component-wise product defined by $(\boldsymbol{u} \circ \boldsymbol{v})_i = u_i v_i$.

Then the functions ϕ_{in} are assumed known with the previously calculated nodal values, and the components of the arbitrary test field are taken under the form $u_i^* = \phi_{in} \chi_{in}^* \psi_{in}$. The same methodology now leads to the following linear system to be solved:

$$\left[\sum_{i=1}^{n_A} (\boldsymbol{\Phi}_n^T \boldsymbol{A}_{1i} \boldsymbol{\Phi}_n) \boldsymbol{A}_{2i} (\boldsymbol{\Psi}_n^T \boldsymbol{A}_{3i} \boldsymbol{\Psi}_n)\right] \boldsymbol{X}_n = \sum_{i=1}^{n_B} \boldsymbol{B}_{2i}[\boldsymbol{B}_{1i}^T \boldsymbol{\Phi}_n \circ \boldsymbol{B}_{3i}^T \boldsymbol{\Psi}_n] \tag{30}$$

Eventually, the functions χ_{in} are assumed known with the previously calculated nodal values, and the components of the arbitrary test field are taken under the form $u_i^* = \phi_{in} \chi_{in} \psi_{in}^*$. The linear system to be solved is:

$$\left[\sum_{i=1}^{n_A} (\boldsymbol{\Phi}_n^T \boldsymbol{A}_{1i} \boldsymbol{\Phi}_n)(\boldsymbol{X}_n^T \boldsymbol{A}_{2i} \boldsymbol{X}_n) \boldsymbol{A}_{3i}\right] \boldsymbol{\Psi}_n = \sum_{i=1}^{n_B} \boldsymbol{B}_{3i}[\boldsymbol{B}_{1i}^T \boldsymbol{\Phi}_n \circ \boldsymbol{B}_{2i}^T \boldsymbol{X}_n] \tag{31}$$

This iteration repeats until convergence. More precisely, by denoting $\boldsymbol{\Phi}_n^{(s)}, \boldsymbol{X}_n^{(s)}, \boldsymbol{\Psi}_n^{(s)}$ the nodal values computed at iteration s, the stagnation criterion reads:

$$\left[\frac{\int_\Omega \|\boldsymbol{\Phi}_n^{(s)} \circ \boldsymbol{X}_n^{(s)} \circ \boldsymbol{\Psi}_n^{(s)} - \boldsymbol{\Phi}_n^{(s-1)} \circ \boldsymbol{X}_n^{(s-1)} \circ \boldsymbol{\Psi}_n^{(s-1)}\|^2 dV}{\int_\Omega \|\boldsymbol{\Phi}_n^{(s-1)} \circ \boldsymbol{X}_n^{(s-1)} \circ \boldsymbol{\Psi}_n^{(s-1)}\|^2 dV}\right]^{1/2} < \delta \tag{32}$$

where δ is a threshold value selected by the user. Alternatively, a maximum number of iterations can be implemented instead in the stagnation loop (see Sect. 3.2.1). The enrichment loop over the number of terms n is stopped when the enrichment criterion is reached:

$$\left[\frac{\int_\Omega \|\boldsymbol{u}_n^{k+1} - \boldsymbol{u}_{n-1}^{k+1}\|^2 dV}{\int_\Omega \|\boldsymbol{u}_1^{k+1}\|^2 dV}\right]^{1/2} < \epsilon \tag{33}$$

where ϵ is another threshold value selected by the user. This criterion leads to a different length of the sum (21) depending on the complexity of the solution at the considered time increment. The selection of its value is discussed in Sect. 3.1.

Relations (29-31) evidence that the same pre-operators $\boldsymbol{A}_{ij}$ and $\boldsymbol{B}_{ij}$ are used throughout the fixed point method to compute the left and right hand sides of the linear systems. Many of them can be computed outside the enrichment loop, and the PGD solver proposed in this paper takes advantage of this property. It then saves numerous operations compared to solvers entirely computing both the left and right hand sides at each iteration of the fixed point method.

2.6 Spatial discretization with spectral elements

In our previous work [21], we used low-order finite elements to solve 2D wave propagation problems with the time adaptive space separation. However, our numerical experiments showed unsatisfactory results for some problems, as presented in Sect. 3.1. It is indeed well known that low-order finite-element methods exhibit poor dispersion properties [4]. To overcome this issue, we employ spectral elements but other high-order discretization schemes (e.g. p-FEM, IGA) could be considered [38]. Spectral elements are high order Lagrangian elements with specific interior points. These latter lead to higher spatial accuracy and reduced dispersion error compared to low-order finite elements [15]. This is a property of primary importance, since spurious high frequency oscillations due to spatial discretization would result in a large number of terms in the separated form. Besides, when the interior points defining the spectral elements are the same as the quadrature points used to numerically evaluate the integrals, the following matrices become diagonal [16]:

$$\mathcal{P} = \int_{\Omega_x} \mathbf{P}(x)\mathbf{P}(x)^T dx \tag{34}$$

$$\mathcal{Q} = \int_{\Omega_y} \mathbf{Q}(y)\mathbf{Q}(y)^T dy \tag{35}$$

$$\mathcal{R} = \int_{\Omega_z} \mathbf{R}(z)\mathbf{R}(z)^T dz \tag{36}$$

This is the so-called nodal quadrature technique, but other lumping strategies can be implemented in a spectral element framework, see for instance [39].

Consequently, the combination of spectral elements, defined on the quadrature points (Gauss-Lobatto-Legendre quadrature is here employed), with the central difference

method, leads to a true explicit time marching scheme. Only trivial and cheap matrix inversions at each time step are then performed. The mass matrix is indeed exactly diagonal in solvers based on spectral elements with the nodal quadrature technique. With standard low-order finite elements, however, the mass matrix must be lumped to get an actual explicit scheme, introducing errors in the numerical procedure [40].

In practice, a polynomial degree between 4 and 10 is employed for wave propagation problems. In order to obtain accurate results, the element size must be selected such that the average number of grid points in the element per minimum wavelength is greater or equal than 5 [16]. As a rule of thumb, for 3D problems discretized in space with the spectral element method and in time with the central difference method, the time step Δt must be selected lower than $0.6\Delta x/c$, with Δx the minimum spacing between two grid points and c the maximum wave velocity in the studied medium.

2.7 Hybrid implicit/explicit time marching schemes

The major limitation of explicit time marching schemes is the stability criterion on the time step Δt which must be selected small enough. As a result, high spatial accuracy, obtained by increasing the number of elements or the polynomial degree, comes with a price to pay in terms of number of time steps, hence of computational time. Implicit schemes, however, are unconditionally stable and the time step should be selected such that the so-called Courant number $c\Delta t/\Delta x$ minimizes the dispersion error introduced by the time discretization [8]. However, implicit schemes involve consistent matrices to be inverted at each time step (the ones related to internal forces), which may become computationally expensive. Moreover, increasing too much the time step can impact the solution accuracy.

To overcome this issue, Quaranta et al. [23] proposed a hybrid implicit/explicit time marching scheme within an in-plane/out-of-plane space separation framework. Their approach consists in simultaneously mimicking an implicit scheme for the out-of-plane 1D problems and an explicit scheme for the in-plane 2D problems. This procedure is illustrated on Fig. 1. The time step is then only constrained by the in-plane spatial discretization. As a result, the solution can be refined through the thickness as needed, without significantly decreasing the time step and affecting the computation time (since only cheap 1D problems are implicit). This numerical behavior is of particular interest for the wave propagation problem we will be dealing with in Sect. 3.3.

In this paper, we slightly improve their hybrid scheme by introducing a parameter $\alpha \geq 0$ which controls amplitude decays and period elongations, as in Newmark's schemes presented in Sect. 2.3. The hybrid scheme, explicit in-plane and implicit out-of-plane, is obtained by selecting α (17), except for the out-of-plane derivatives of the displacement field that are treated implicitly:

$$u_{i,z}^{k} \leftarrow \alpha u_{i,z}^{k+1} + (1-2\alpha)u_{i,z}^{k} + \alpha u_{i,z}^{k-1} \tag{37}$$

Consequently, the matrix operators $\boldsymbol{A}_{1i}$ and $\boldsymbol{A}_{2i}$ are diagonal, as with the central difference method, hence the resolution of the linear systems (29-30) is explicit. On the other hand, the matrix operators $\boldsymbol{A}_{3i}$ related to the terms $u_{i,z}^{k}$ are not diagonal, and the resolution of the linear system (31) is implicit, as with a Newmark's scheme with $\alpha \neq 0$. These latter are unconditionally stable if $\alpha \geq 1/4$, but our numerical experiments showed that the proposed hybrid scheme is unconditionally stable if $\alpha > 1/4$.

3 Numerical results

Three numerical tests are considered in order to validate the method. In the first test, a two dimensional problem is studied to check the spectral convergence with the space separation. In the second, a three dimensional Lamb's test in an isotropic linear elastic medium is studied. The numerical performances of the in-plane/out-of-plane and full space separations are compared. In the last test, a laser shock configuration on a CFRP target is studied with the in-plane/out-of-plane separation. The performances of the hybrid explicit in-plane/implicit out-of-plane time marching scheme are illustrated. All the simulations are run with Matlab R2018a on a laptop with a single core Intel i7-5500U 2.40 GHz CPU and 8 GB RAM. Spectral elements are implemented from an open-source package [41].

3.1 Spectral convergence and enrichment criterion

Spectral elements provide higher accuracy than low-order finite elements for the same number of discretization points. In order to check this property within the proposed space separation framework, the two dimensional test case extensively studied in [42] is considered. It consists in a linear elastic medium, initially at rest, occupying a rectangular geometry with dimensions 2m $\times$ 1m. Dummy mechanical properties are used: the shear modulus is $G = 1$Pa, the density is $\rho = 1$kg/m^3 and the Poisson's ratio is $\nu = 1/3$. The left edge of the domain is subjected to a uniformly distributed pressure:

$$p(t) = \sin(2\pi f_0 t)\exp(-(t-t_0)^2/(2\tau^2)) \tag{38}$$

with $f_0 = 1$Hz, $t_0 = 1$s and $\tau = 4$s. All other edges are free of traction. The time interval of interest is [0s, 25s]. Initial conditions are null.

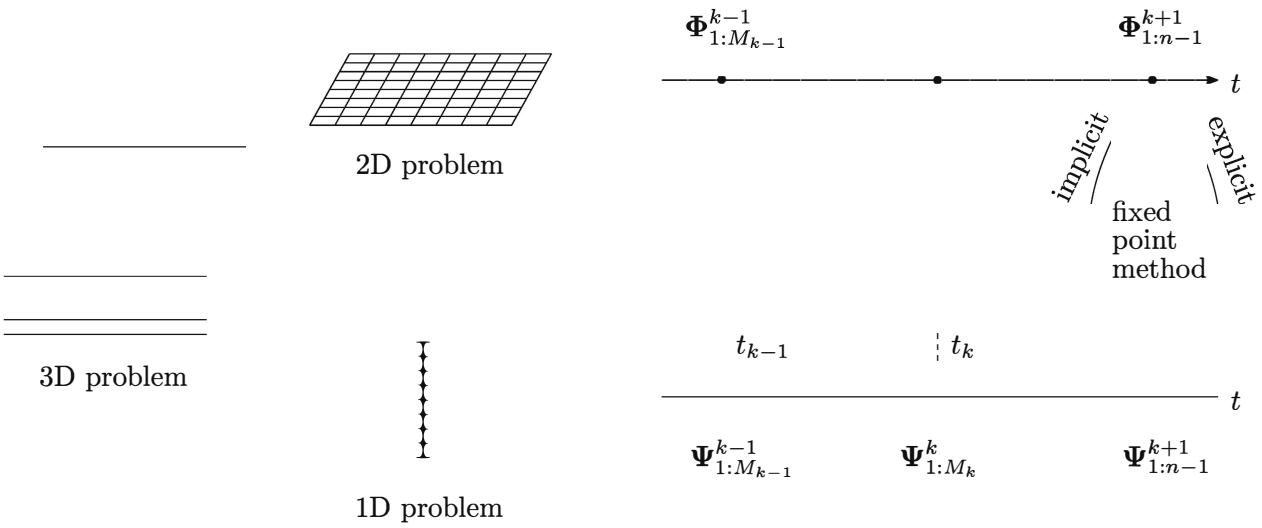

Fig. 1 Illustration of the explicit in-plane/implicit out-of-plane hybrid scheme with the 2D/1D time adaptive space separation. See Appendix for notations

An observation point A is considered at the middle of the right edge of the domain. The objective is to compare the horizontal displacement $u_1(A,t)$ for different numerical solutions with a reference solution. This latter is computed with a standard 2D SEM solver with a grid of 20×10 spectral elements of degree 10 (60,903 degrees of freedom). FEM simulations are carried out with fully integrated 4-nodes elements and a lumped mass matrix. All the solutions are computed with 32, 000 time steps with the central difference method. The time step is then small enough to ensure that numerical errors are mainly due to spatial discretization or space separation. The error indicator considered in this study is:

$$\text{error} = \frac{\|\mathbf{u}_1 - \mathbf{u}_1^{\text{ref}}\|}{\|\mathbf{u}_1^{\text{ref}}\|} \tag{39}$$

where $\mathbf{u}_1$ and $\mathbf{u}_1^{\text{ref}}$ are the numerical and reference solutions (observed at point A) discretized in time, respectively.

Figure 2 compares the errors obtained with a 2D FEM solver or a 2D SEM solver (without space separation). The FEM solutions are computed by refining the mesh with more square elements. The SEM solutions are computed with a 4×2 grid of spectral elements by increasing the polynomial degree of the shape functions. The 2D SEM solver outperforms the 2D FEM solver on this example. An error of 10^{-2} is obtained with 273 degrees of freedom (DOFs) with the 2D SEM solver, while 60, 903 DOFs are required with the 2D FEM solver to reach the same error level. However, it must be mentioned that the discrepancy between FEM and SEM error levels is usually less severe in more complex situations [42].

The influence of the space separation is then investigated depending on the enrichment criterion given by relation (33). Figure 3 compares the errors obtained with PGD solutions computed with a 1D/1D space separation and spectral elements. It can be seen that the rate of convergence depends on the selection of the enrichment criterion. This latter can be viewed as an a priori error indicator. Spectral convergence is indeed recovered (superposition with the 2D SEM curve) up to polynomial degree P if the enrichment criterion is selected lower or equal than 10^{-P}. The value $\epsilon = 10^{-P}$ is then selected for all our numerical tests presented hereunder.

A consequence of the faster convergence rate with spectral elements is that a smaller number of terms is computed to reach a given error level. For instance, 10 terms are computed (in average) to reach the error level of 10^{-2} with 1D/1D SEM (with an equivalent grid of 4×2 spectral elements of degree 5 and $\epsilon = 10^{-5}$), while 80 terms are computed (in average) with 1D/1D FEM to reach the same error level (with an equivalent grid of 100×50 4-nodes finite elements and $\epsilon = 10^{-4}$). As a result, more accurate solutions are computed with less computational effort.

3.2 3D Lamb's test

Lamb's problem is an important numerical test to validate a solver for elastic wave propagation. It consists in applying a transient concentrated loading on the surface of an infinite half-space occupied with an isotropic elastic material. This configuration generates P-waves (longitudinal) and S-waves (transverse) in the volume, and R-waves in the surface (Rayleigh waves). The analytical solution of this problem shows that R-waves are non dispersive and have a strong amplitude with respect to volume waves [43]. To simulate

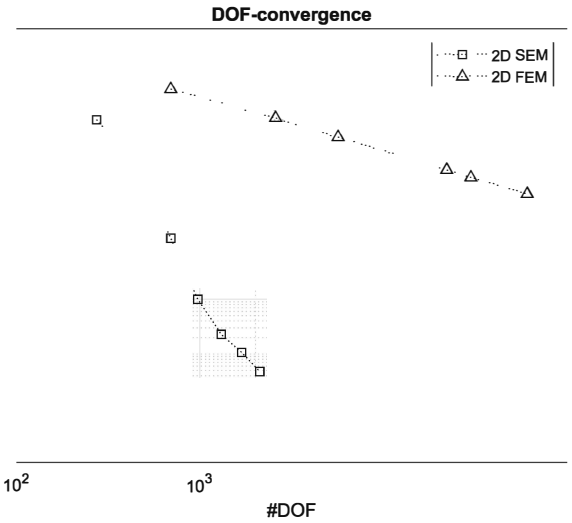

Fig. 2 Error evolution obtained with 2D FEM and 2D SEM solvers with respect to a reference numerical solution computed with a grid of 20×10 spectral elements of degree 10 (60,903 degrees of freedom)

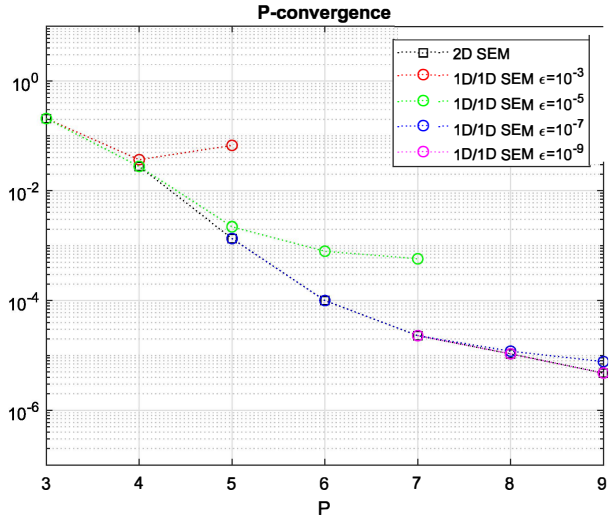

Fig. 3 Error evolutions obtained with a PGD solver based on a 1D/1D space separation and spectral elements

Lamb's problem, a Ricker's source is applied:

$$f(t) = -A(2\pi^2(t-t_s)^2/t_p^2 - 1)\exp(-\pi^2(t-t_s)^2/t_p^2) \tag{40}$$

with $A = 2.10^6$N, $t_s = 2.9$s, and $t_p = 3$s (see Fig. 4). The material characteristics are $E = 10$MPa, $\nu = 0.24$ and $\rho = 1700$kg/m^3, as in [30] for comparison purposes. The numerical domain is a hexahedron with dimensions 300m $\times$ 300m $\times$ 300m. Due to the problem's symmetry, the 3D solutions are actually computed on one fourth of the physical domain by prescribing appropriate Dirichlet boundary conditions ($\mathbf{u} \cdot \mathbf{n} = 0$ on a truncated surface with normal $\mathbf{n}$). Either free surface boundary conditions or P-ABCs are

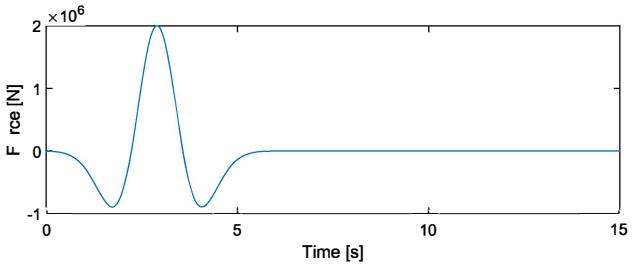

Fig. 4 Ricker's source applied at (0m, 0m, 300m)

implemented on the side and bottom surfaces of the numerical model. Initial conditions are null.

3.2.1 Comparison of space separation techniques

First we compare the results obtained with the in-plane/out-of-plane and full space separation. Two observation points A and B are considered: A is located on the surface at position (50m, 0m, 300m), and B is located in the volume at position (0m, 0m, 250m). The time interval of interest is such that spurious wave reflections at numerical boundaries do not reach the observation points. Under this condition and given the symmetry of Lamb's problem, a 2D axisymmetric numerical reference solution is computed with LS-DYNA Explicit v7.1. A sufficiently converged mesh of 300×300 4-node axisymmetric finite elements is used (270,000 DOFs), and the time step is equal to 7.46ms.

Figure 5 compares the solutions obtained with the in-plane/out-of-plane separation (2D/1D curves) and the full separation (1D/1D/1D curves). In each case, the spatial discretization is equivalent to a uniform grid of 729 3D spectral elements of degree 4 (151, 959 DOFs). In the full separation, a $9 \times 9 \times 9$ grid of 1D spectral elements is used. In the in-plane/out-of-plane separation, a 9×9 grid of 2D spectral elements is used for the in-plane problems, and a grid of 9 1D elements is used for the out-of-plane problems. Following the guideline provided in the previous section, the enrichment criterion is selected equal to 10^{-4}. A maximum number of 10 iterations is implemented in the stagnation loop as recommended in our previous work [21]. The central difference method is employed for the time integration ($\alpha = 0$) and a uniform time step of 34.6ms is used. The number of time steps is 212. The two space separation techniques provide very similar results, with a relative error with respect to the reference solution around 1% on the vertical component of the displacement field.

Figure 6 shows 3D snapshots of a numerical solution computed with the 2D/1D separation and P-ABCs, on a longer time interval. As expected, we observe both volume and surface waves. The surface wave is non dispersive and stronger in magnitude than the volume waves. The P-ABCs perform well and reduce spurious reflections.

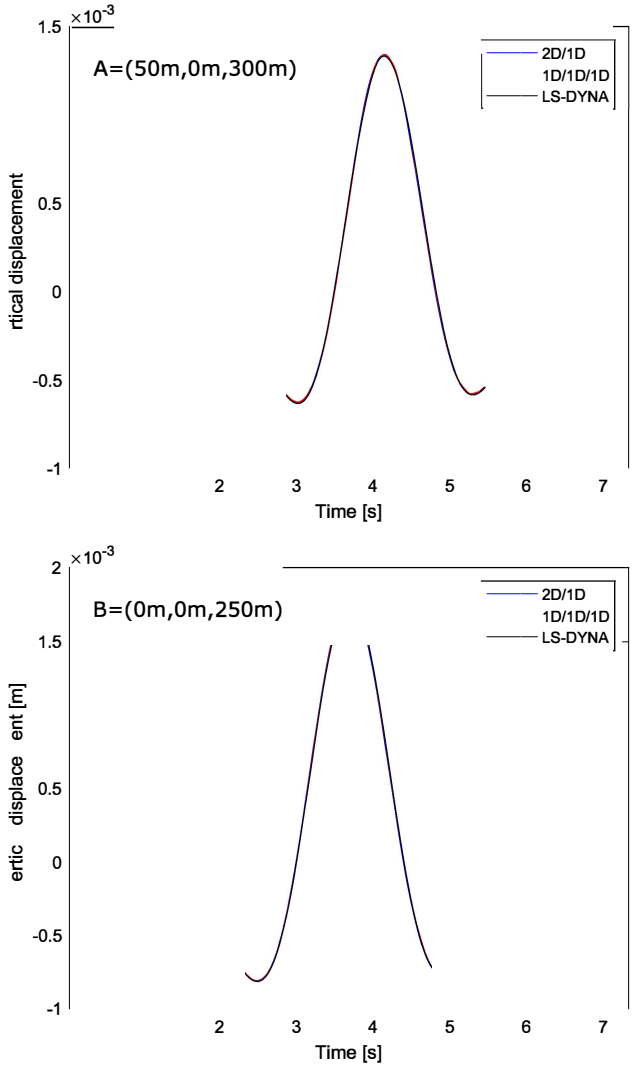

Fig. 5 Comparison of the vertical displacement computed at observation point A (top) and B (bottom)

Surprisingly, the full space separation demands much more computation time than the 2D/1D separation. Even if only cheap 1D problems are solved, it appears that the large number of terms involved in the solution increases the memory needs, which slows down the computation with the employed calculation ressources. Figure 7 presents the evolution of the number of terms in the numerical solutions throughout the simulation. An average number of 206 terms is required in the 1D/1D/1D solution with a total computation time of 4145s (17.8s per time step in average). On the other hand, the 2D/1D separation achieves satisfactory performances, with only 14 terms in average and a total computation time of 248s (1.07s per time step in average). As reported in [21], the number of terms increases as the waves expand in the domain (up to 527 with the full separation and up to 19 with the in-plane/out-of-plane separation).

3.2.2 Computation time

The numerical performances of the 2D/1D separation are now explored by enlarging the numerical domain while keeping the same grid point spacing. In contrast to standard 3D solvers, the way of increasing the number of grid points with a space separation technique has an effect on the computation time. Three spatial enlargements are considered: enlargement in z-direction (out-of-plane), enlargement in x, y-directions (in-plane), and enlargement in all directions (volume). Numerical solutions are computed with the parameters of previous section, on the same time interval, but with different spatial domain sizes. As a result, all the simulations compute the same solutions with the same spatial resolution, but within spatial domains of different sizes.

Figure 8 summarizes the evolution of the average computation time (CPU time) per time step depending on the way of enlarging the spatial domain (out-of-plane, in-plane or volume enlargements). First, it can be appreciated that large simulations with more than one million of DOFs are efficiently computed with Matlab and a personal laptop. Full 3D calculations with as many DOFs simply cannot be conducted with Matlab and the laptop used in this study. Yet, with the proposed approach the CPU time per time step is at most equal to 5.7s for the largest simulation (1,594,320 DOFs). It must be mentioned that the average CPU time per time step would increase for the largest domains if the simulation time was increased. It is indeed reported in [21] that the number of terms in the solution (hence the CPU time per time step) increases as the waves expand in the domain and then it stabilizes.

Second, the curve obtained with the out-of-plane enlargement is linear and below the polynomial curve obtained with the in-plane enlargement. It means that the CPU time per time step linearly increases with the number of DOFs when the domain is enlarged in the out-of-plane direction. This would not be the case with a standard 3D solver since the way of increasing the DOFs does not have an influence (the curve would be polynomial). The curve associated to the volume enlargement is polynomial and in between the two other curves. This can easily be explained as follows. In the out-of-plane enlargement, only the size of the 1D problems is increased, while in the in-plane enlargement it is the size of the 2D problems that is increased. In the volume enlargement, the sizes of both the 1D and 2D problems is increased, which leads to a polynomial curve as well, but below the curve of the in-plane enlargement since for a same number of DOFs the size of the 2D problems is smaller.

As a conclusion, the 2D/1D separation allows enlarging the domain in the out-of-plane direction without significantly affecting the computation time. The number of terms in the solution remained moderate for all the numerical tests performed on this test case (below 20). The resolution of the

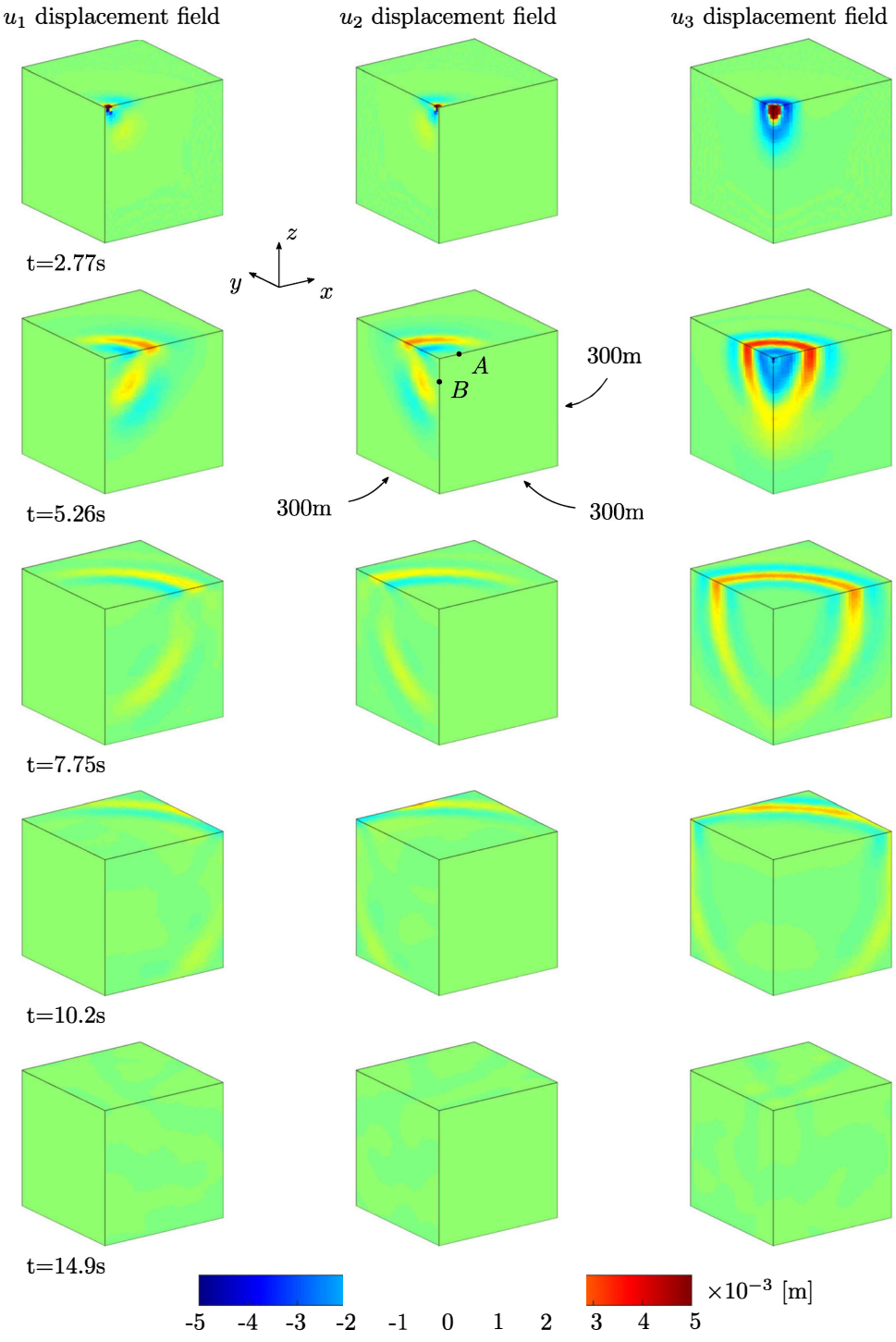

Fig. 6 Snapshots of the numerical solution computed with the 2D/1D space separation and a $10 \times 10 \times 10$ mesh of spectral elements of degree 4 (206,763 DOFs). P-ABCs are implemented to reduce spurious reflections

in-plane problems is fast thanks to the spectral discretization enabling a true explicit scheme. However, the 1D/1D/1D separation is less effective on this test case. The concentrated loading generates radial waves challenging the full space separation. It results in a large number of terms in the numerical solution (roughly the square of the number of terms obtained with the 2D/1D separation). Consequently, more memory is needed to handle the numerous pre-operators to be stored to compute the right hand sides of the linear systems (29-31), which demands more computation time.

3.3 Laser shock on a composite laminate target

The last numerical test is inspired from a laser shock configuration on a composite laminate target. The target consists in a stacking sequence of five (0°, 90°) CFRP plies (140μm

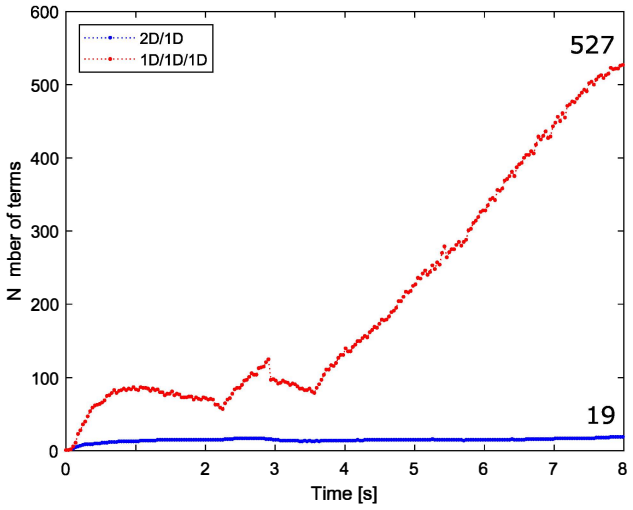

Fig. 7 Evolution of the number of terms in the numerical solutions throughout the simulation depending on the space separation technique

thick) separated with epoxy interplies (30μm thick), see Figure 9a. The dimensions of the target are 8mm × 8mm × 1.7mm and the material properties are given in Tables 1-2. A sudden pressure pulse of 150MPa is applied on a circular spot on the top surface of the target, see Figure 9b. The bottom and side surfaces are free of traction. The time interval of interest is [0,1.95]μs to avoid spurious reflections on the side surfaces of the target (to assume free surface boundary conditions). Initial conditions are null. It must be mentioned that P-ABCs would not perform well with this layered medium, because of the numerous crossings of interfaces and corners that are known to deteriorate absorbing performances [44]. More efficient ABCs should be implemented to improve the accuracy on larger time intervals of interest, see Sect. 2.1.

We solve this problem with the hybrid explicit in-plane/implicit out-of-plane scheme with $\alpha = 0.3$. The 2D/1D space separation is employed. The numerical model is designed as follows. Frequencies up to 4.5MHz are significantly excited with this time loading (at least 3% of maximum spectrum amplitude). The minimum wave speed in this layered medium is 598m/s (transverse wave propagating perpendicular to fiber orientation), hence the minimum wavelength we want to resolve is 133μm. As mentioned in Sect. 2.7, at least 5 grid points per minimum wavelength must be used in order to have enough spatial resolution. With spectral elements of degree 4, this criterion results in an element size of maximum 106μm. To comply with this criterion, the in-plane mesh is a grid of 80 × 80 spectral elements of degree 4 (174,243 in-plane DOFs). The in-plane problems are treated explicitly hence the time step is selected equal to 1.82ns to satisfy the stability condition (Courant number equal to 0.5). In the out-of-plane direction, 3 spectral elements of degree 4 are used per CFRP ply, and 1 spectral element of degree 2 is used per Epoxy interply (417 out-of-plane DOFs). The out-of-plane

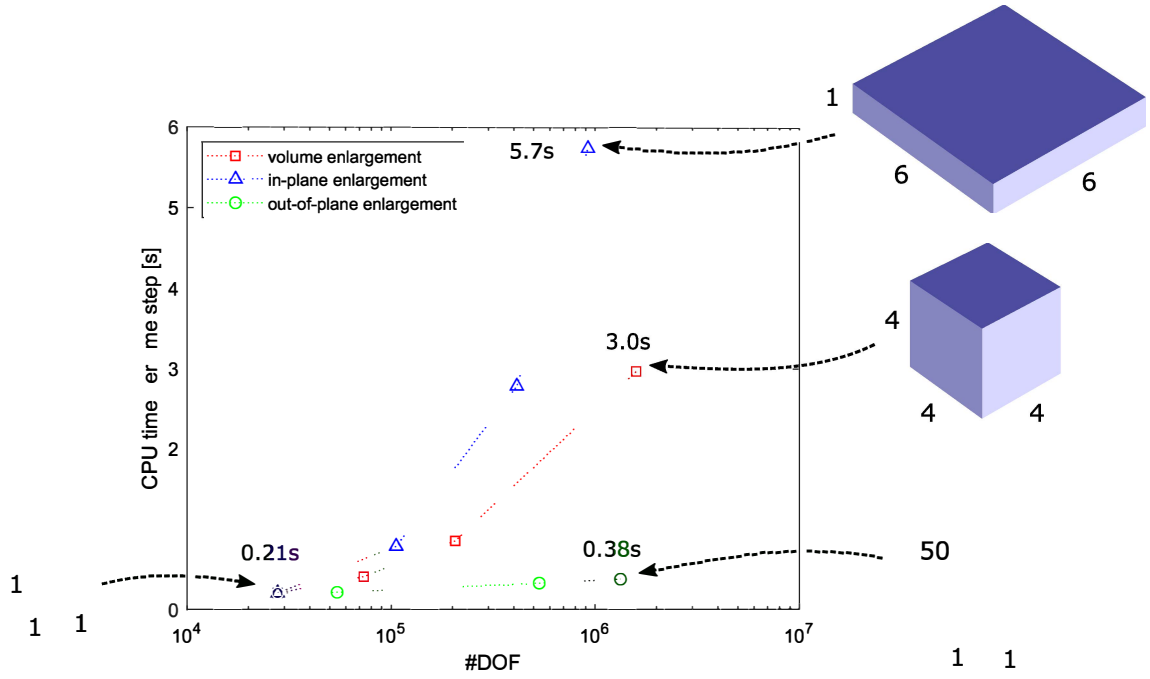

Fig. 8 Evolution of the average CPU time per time step depending on the way of increasing the number of DOFs. Numbers next to the edges of the hexahedral domains indicate the scaling factors from the reference domain 300m × 300m × 300m discretized with a grid of 5 × 5 × 5 spectral elements of degree 4 (27,783 DOFs). The same spatial resolution is used for each simulation

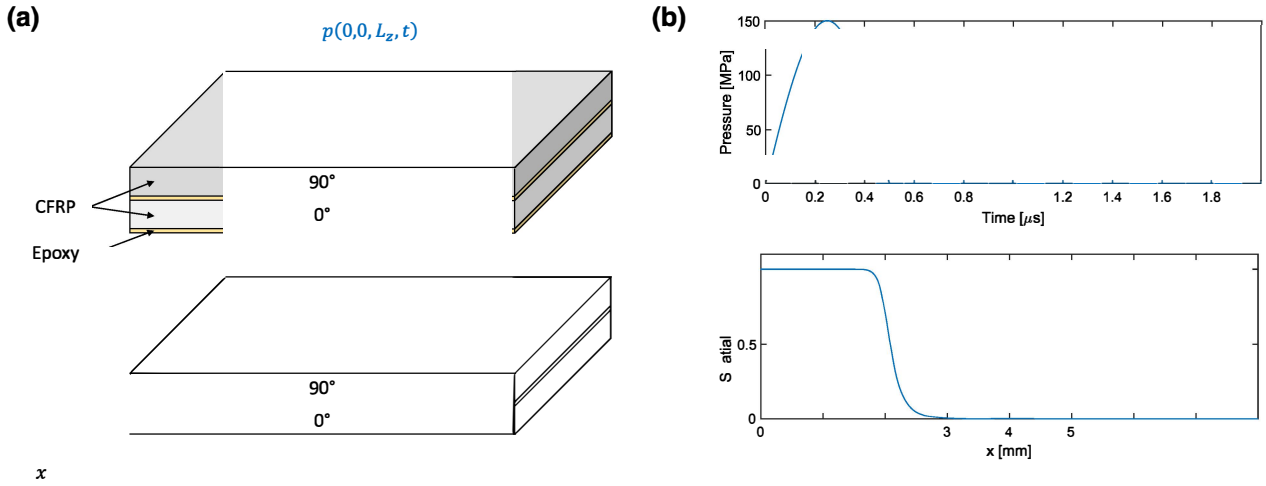

Fig. 9 **a** Stacking configuration. CFRP plies thickness is 140μm and Epoxy interplies thickness is 30μm. **b** Time and spatial profiles of the applied loading

Table 1 Mechanical properties of epoxy interplies

E (GPa)	ν	ρ (kg/m^3)
5.2	0.35	1260

spatial resolution is richer than the in-plane spatial resolution (5 points per minimum wavelength for the in-plane problems and 13 for the out-of-plane problems). The total number of DOFs of this 3D problem is 24,219,777. Thanks to the hybrid scheme, the out-of-plane problems are treated implicitly with the coarser time step imposed by the in-plane discretization. If the central difference method ($\alpha = 0$) was used instead of the hybrid scheme, the stability condition would impose a finer time step equal to 0.53ns, hence to 3,676 time steps instead of 1, 072 with the hybrid scheme. Table 3 summarizes the model parameters.

Figure 10 displays snapshots of the propagating stress fields at different instants. As expected, the applied pressure of 150MPa generates a compressive σ_{33} wave propagating through the thickness. The nature of this wave (compressive or tensile) is reverted at each reflection on the top or bottom faces of the target which are free of traction (the loading is null before the return of this wave on the top face). The inspection of σ_{11} and σ_{22} stress fields reveal the anisotropy of the CFRP plies: waves are stronger and faster along fiber orientation (fibers on top of the target are aligned in y-direction). Edge effects are also clearly visible on the top face of the target with σ_{11} and σ_{22} ripples propagating from the discontinuity of the spatial loading. It is observed that the reflection of the σ_{33} main wave on the top face reloads σ_{11} and σ_{22} waves.

Table 2 Mechanical properties of CFRP plies. Data extracted from [45]

E_1 (GPa)	E_2 (GPa)	E_3 (GPa)	ν_{12}	ν_{12}	ν_{12}	G_1 (GPa)	G_2 (GPa)	G_3 (GPa)	ρ (kg/m^3)
72.9	22.9	9.70	0.77	0.0187	0.218	48.4	0.873	0.558	1563

Table 3 2D/1D model parameters

#DOFs	24,219,777
Number of time steps	1,072
In-plane mesh	80 × 80 spectral elements of degree 4
Out-of-plane mesh	CFRP ply: 3 spectral elements of degree 4 Epoxy interply: 1 spectral element of degree 2
Enrichment criterion	$\epsilon = 10^{-4}$
Stagnation criterion	10 iterations
Time marching scheme	hybrid scheme with $\alpha = 0.3$

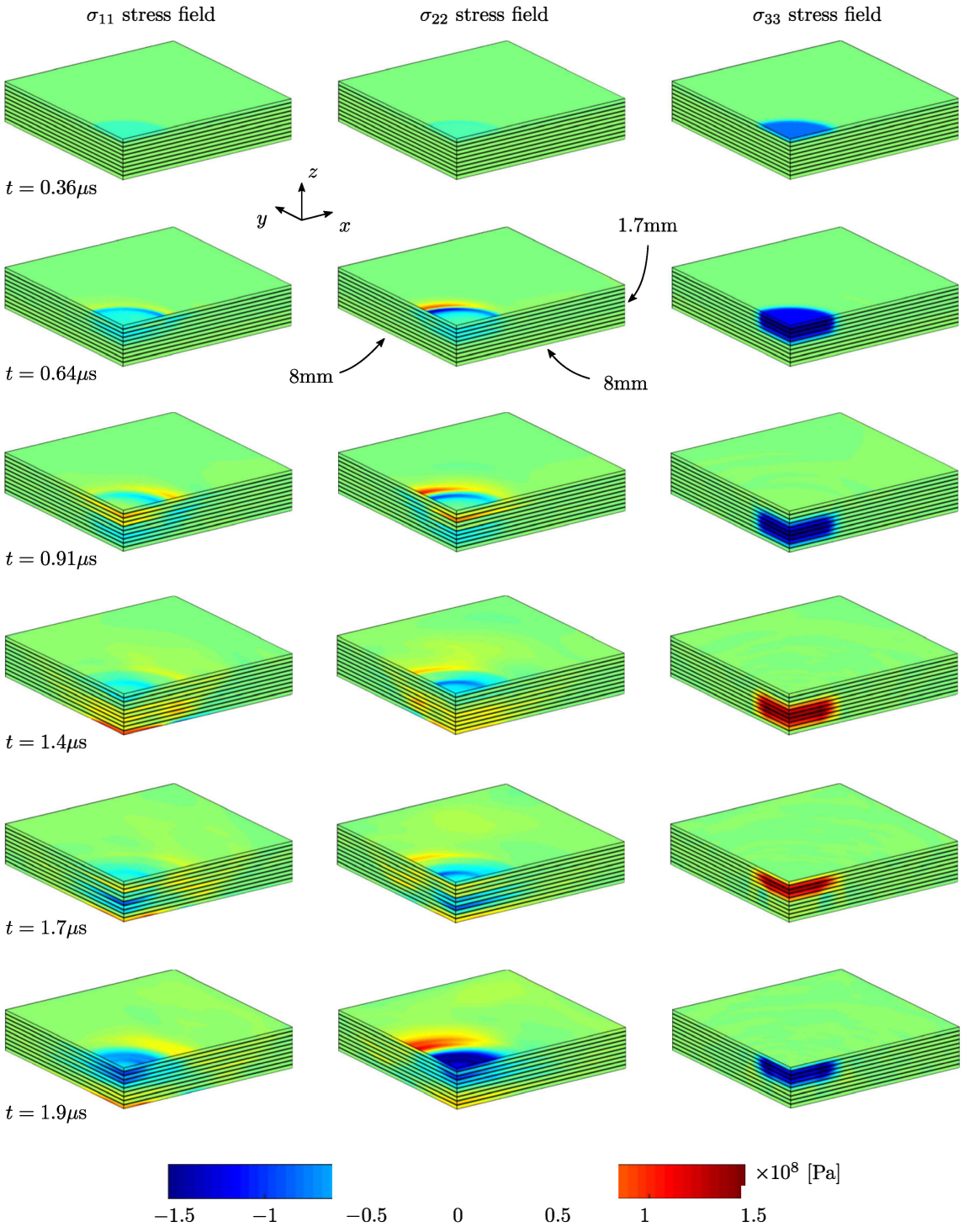

Fig. 10 Snapshots of σ_{11} (left), σ_{22} (middle) and σ_{33} (right) stress fields at different instants

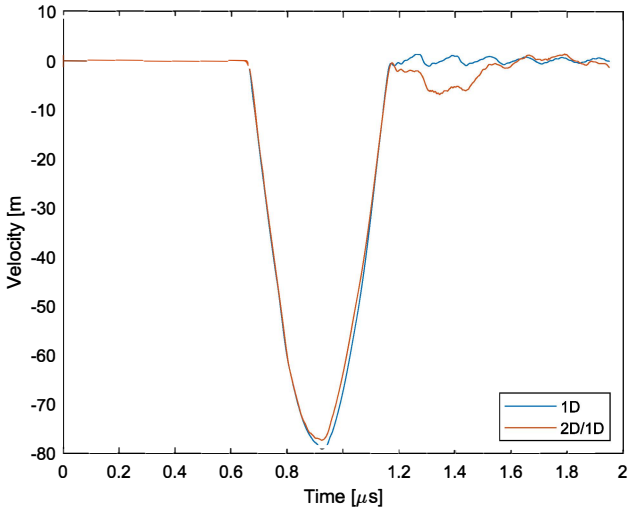

Fig. 11 Back face velocity computed with a 1D model and a 2D/1D model

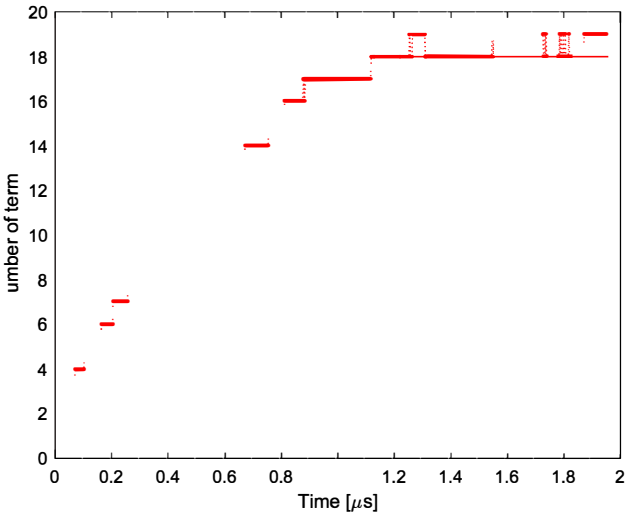

Fig. 12 Evolution of the number of terms through the simulation with the 2D/1D model

Eventually, Figure 11 compares the back face velocities (observation at the middle of bottom face) computed with the 2D/1D model and a 1D model using the same spectral discretization along z-axis. This latter is based on a 1D scalar wave equation with varying mechanical properties:

$$\rho(z)\ddot{u}(z,t) = E(z)\partial_z^2 u(z,t) \tag{41}$$

where $E(z)$ and $\rho(z)$ are the Young modulus and density fields of the 3D model along z-axis, respectively.

The peak amplitude of the 3D calculation is slightly lower because of the three-dimensional expansion of the waves. The scattering patterns due to the plies (visible from $t = 1.2\mu$s) are different because edge effects are not taken into account in the 1D model. The ripples following the main peak would be larger if the width of the σ_{33} wave was smaller compared to the plies thicknesses.

In terms of numerical performances, the average number of terms throughout the simulation is 14.4 and the computation time is 17.9 hours (50s per time step in average). The number of terms in the solution stabilizes around 18, see Figure 12. It can be appreciated that such a large simulation (24,219,777 DOFs and 1,072 time steps) has been successfully conducted with Matlab R2018a and a personal laptop.

4 Conclusion

In this work, we presented space separation techniques to speed up wave propagation simulations in three-dimensional plate domains. High order spectral elements are employed instead of low-order finite elements to improve the convergence and dispersion properties that are of primary importance for such problems. Spectral convergence is retriev with an adequate selection of the enrichment criterion in the Proper Generalized Decomposition algorithm. More compact separated representations are then obtained to reach a given error level. The full space separation is found less effective in terms of computation time than the in-plane/out-of-plane separation for the considered test cases. The proposed framework enables true hybrid time marching schemes, simultaneously implicit or explicit throughout the fixed point method depending on the spatial directions. The solution can then be improved through one direction as needed, without decreasing the time step or affecting the computation time. This behavior is promising for wave propagation simulations in composite laminate media characterized by strong material properties variations through the thickness. Numerical experiments on three-dimensional test cases confirm the desired behavior of the proposed method: 3D problems with millions of degrees of freedom are solved with computational ressources characteristic of 2D problems. Future work will be devoted to the implementation of accurate absorbing boundary conditions for composite laminate media.

Acknowledgements This work was supported by a government funding under the project FUI MONARQUE France.

Appendix

Particular attention is required on the manipulation of the PGD matrix operators for wave propagation problems. The number of terms in the solutions is indeed generally larger than with other elastodynamic problems, since small wavelengths are significantly excited by the applied loading generating the waves. As a result, many matrix-vector prod-

ucts must be computed in the terms involving $\mathbf{u}_n^{k+1}$, $\mathbf{u}^k$ and $\mathbf{u}^{k-1}$ in relation (17). It is even worse if the medium is anisotropic since more elastic coefficients are non null in the elastic tensor $\mathbf{C}$. As proposed in [21], we avoid unnecessary operations by computing $\mathbf{A}_{ij}$ and $\mathbf{B}_{ij}$ in (29-31) outside the enrichment loop of the fixed point method.

The component-wise product between two vectors $\mathbf{u}$ and $\mathbf{v}$ is defined by $(\boldsymbol{u} \circ \boldsymbol{v})_i = u_i v_i$. The following vectorization property is employed:

$$\sum_{i=1}^{M} (\boldsymbol{\Phi}^T \mathbf{A} \boldsymbol{\Phi}_i)(\boldsymbol{X}^T \mathbf{B} \boldsymbol{X}_i)(\boldsymbol{\Psi}^T \mathbf{C} \boldsymbol{\Psi}_i) = (\boldsymbol{\Phi}^T \boldsymbol{\mathcal{A}})[\boldsymbol{\mathcal{B}}^T \boldsymbol{X} \circ \boldsymbol{\mathcal{C}}^T \boldsymbol{\Psi}] \tag{42}$$

where $\mathbf{A}$, $\mathbf{B}$, $\mathbf{C}$ are matrices and $\boldsymbol{\Phi}$, $\boldsymbol{\Phi}_i$, $\boldsymbol{X}$, $\boldsymbol{X}_i$, $\boldsymbol{\Psi}$, $\boldsymbol{\Psi}_i$ are vectors of appropriate dimensions, and:

$$\boldsymbol{\mathcal{A}} = \mathbf{A} \boldsymbol{\Phi}_{i=1:M} \tag{43}$$

$$\boldsymbol{\mathcal{B}} = \mathbf{B} \boldsymbol{X}_{i=1:M} \tag{44}$$

$$\boldsymbol{\mathcal{C}} = \mathbf{C} \boldsymbol{\Psi}_{i=1:M} \tag{45}$$

where we noted $\boldsymbol{\Phi}_{i=1:M} = [\boldsymbol{\Phi}_1 | \ldots | \boldsymbol{\Phi}_M]$, $\boldsymbol{X}_{i=1:M} = [\boldsymbol{X}_1 | \ldots | \boldsymbol{X}_M]$ and $\boldsymbol{\Psi}_{i=1:M} = [\boldsymbol{\Psi}_1 | \ldots | \boldsymbol{\Psi}_M]$.

We present hereunder how is computed one of the terms of (17) with $u_i^* = \phi_{in}^* \chi_{in} \psi_{in}$. For simplicity we assume $\rho = \rho(z)$. First we use the separated form of the solution:

$$\int_\Omega \rho \mathbf{u}^* \cdot \mathbf{u}^k dV \approx \sum_{i=1}^{3} \sum_{j=1}^{M_k} \int_{\Omega_x} \phi_{in}^* \phi_{ij}^k dx \int_{\Omega_y} \chi_{in} \chi_{ij}^k dy \int_{\Omega_z} \rho \psi_{in} \psi_{ij}^k dz \tag{46}$$

Then we use the nodal approximations (22-24):

$$\int_\Omega \rho \mathbf{u}^* \cdot \mathbf{u}^k dV \approx \sum_{i=1}^{3} \sum_{j=1}^{M_k} (\boldsymbol{\Phi}_{in}^{*T} \boldsymbol{\mathcal{P}} \boldsymbol{\Phi}_{ij}^k)(\boldsymbol{X}_{in}^T \boldsymbol{\mathcal{Q}} \boldsymbol{X}_{ij}^k)(\boldsymbol{\Psi}_{in}^T \boldsymbol{\mathcal{R}}(\rho) \boldsymbol{\Psi}_{ij}^k) \tag{47}$$

where matrices $\boldsymbol{\mathcal{P}}$ and $\boldsymbol{\mathcal{Q}}$ are given by relations (34-35), respectively, and $\boldsymbol{\mathcal{R}}(\rho) = \int_{\Omega_z} \rho(z) \mathbf{R}(z) \mathbf{R}(z)^T dz$. Then property (42) leads to the desired form:

$$\int_\Omega \rho \mathbf{u}^* \cdot \mathbf{u}^k dV \approx \sum_{i=1}^{3} (\boldsymbol{\Phi}_n^{*T} \boldsymbol{B}_{1i})[\boldsymbol{B}_{2i}^T \boldsymbol{X}_n \circ \boldsymbol{B}_{3i}^T \boldsymbol{\Psi}_n] \tag{48}$$

with $\boldsymbol{\Phi}_n^* = (\boldsymbol{\Phi}_{1n}^*, \boldsymbol{\Phi}_{2n}^*, \boldsymbol{\Phi}_{3n}^*)$. The expressions of the matrices $\boldsymbol{B}_{1i}$, $\boldsymbol{B}_{2i}$ and $\boldsymbol{B}_{3i}$ for $i = 1$ are:

$$\boldsymbol{B}_{11} = \begin{bmatrix} \boldsymbol{\mathcal{P}} \boldsymbol{\Phi}_{i=1:M_k}^k & \mathbf{0}_x & \mathbf{0}_x \\ \mathbf{0}_x & \mathbf{0}_x & \mathbf{0}_x \\ \mathbf{0}_x & \mathbf{0}_x & \mathbf{0}_x \end{bmatrix}$$

$$\boldsymbol{B}_{21} = \begin{bmatrix} \boldsymbol{\mathcal{Q}} \boldsymbol{X}_{i=1:M_k}^k & \mathbf{0}_y & \mathbf{0}_y \\ \mathbf{0}_y & \mathbf{0}_y & \mathbf{0}_y \\ \mathbf{0}_y & \mathbf{0}_y & \mathbf{0}_y \end{bmatrix}$$

$$\boldsymbol{B}_{31} = \begin{bmatrix} \boldsymbol{\mathcal{R}}(\rho) \boldsymbol{\Psi}_{i=1:M_k}^k & \mathbf{0}_z & \mathbf{0}_z \\ \mathbf{0}_z & \mathbf{0}_z & \mathbf{0}_z \\ \mathbf{0}_z & \mathbf{0}_z & \mathbf{0}_z \end{bmatrix}$$

where $\mathbf{0}_x$, $\mathbf{0}_y$, $\mathbf{0}_z$ are null matrices with appropriate dimensions. For $i = 2, 3$ the expressions are similar with shifted diagonal blocks.

References

1. Ehrhart B, Ecault R, Touchard F, Boustie M, Berthe L, Bockenheimer C, Valeske B (2014) Development of a laser shock adhesion test for the assessment of weak adhesive bonded CFRP structures. Int J Adhesion Adhesives 52:57–65. https://doi.org/10.1016/j.ijadhadh.2014.04.002
2. Sagnard M, Ecault R, Touchard F, Boustie M, Berthe L (2019) Development of the symmetrical laser shock test for weak bond inspection. Opt Laser Technol 111:644–652. https://doi.org/10.1016/j.optlastec.2018.10.052
3. Ecault R, Touchard F, Berthe L, Boustie M (2020) Laser shock adhesion test numerical optimization for composite bonding assessment. Compos Struct 247:112441. https://doi.org/10.1016/j.compstruct.2020.112441
4. Marfurt KJ (1984) Accuracy of finite-difference and finite-element modeling of the scalar and elastic wave equations. Geophysics 49(5):493–682. https://doi.org/10.1190/1.1441689
5. Ihlenburg F, Babuška I (1995) Dispersion analysis and error estimation of Galerkin finite element methods for the Helmholtz equation. Int J Numer Meth Eng 38:3745–3774. https://doi.org/10.1002/nme.1620382203
6. Schmicker D, Duczek S, Liefold S, Gabbert U (2014) Wave propagation analysis using high-order finite element methods: spurious oscillations excited by internal element eigenfrequencies. Technische Mechanik—Scientific Journal for Fundamentals and Applications of Engineering Mechanics 34:51–71. https://doi.org/10.24352/UB.OVGU-2017-053
7. Gibson PC (2014) The combinatorics of scattering in layered media. SIAM J ApplMath 74(4):919–938. https://doi.org/10.1137/130923075
8. Noh G, Ham S, Bathe K-J (2013) Performance of an implicit time integration scheme in the analysis of wave propagations. Comput Struct 123:93–105. https://doi.org/10.1016/j.compstruc.2013.02.006
9. Fung T (2003) Numerical dissipation in time-step integration algorithms for structural dynamic analysis. Prog Struct Engng Mater 5:167–180. https://doi.org/10.1002/pse.149
10. Beskos DE (1987) Boundary element methods in dynamic analysis. Appl Mech Rev 40(1):1–23. https://doi.org/10.1115/1.3149529

11. Bouchon M, Schultz C, Toksöz M (1996) Effect of three-dimensional topography on seismic motion. J Geophys Res 101:5835–5846
12. Hulbert GM, Hughes TJ (1990) Space-time finite element methods for second-order hyperbolic equations. Comput Methods Appl Mech Eng 84(3):327–348. https://doi.org/10.1016/0045-7825(90)90082-W
13. Richter G (1994) An explicit finite element method for the wave equation. Appl Numer Math 16(1):65–80. https://doi.org/10.1016/0168-9274(94)00048-4
14. Seriani G, Priolo E (1994) Spectral element method for acoustic wave simulation in heterogeneous media. Finite Elements Anal Des 16(3):337–348. https://doi.org/10.1016/0168-874X(94)90076-0
15. Komatitsch D, Vilotte J-P, Vai R, Castillo-Covarrubias J, Sánchez-Sesma F (1999) The spectral element method for elastic wave equations–application to 2-D and 3-D seismic problems. Int J Numer Meth Engng 45:1139–1164. https://doi.org/10.1002/(SICI)1097-0207(19990730)45:9<1139::AID-NME617>3.0.CO;2-T
16. Komatitsch D, Tromp J (1999) Introduction to the spectral element method for three-dimensional seismic wave propagation. Geophys J Int 139(3):806–822. https://doi.org/10.1046/j.1365-246x.1999.00967.x
17. Dauksher W, Emery A (1997) Accuracy in modeling the acoustic wave equation with Chebyshev spectral finite elements. Finite Elements Anal Des 26(2):115–128. https://doi.org/10.1016/S0168-874X(96)00075-3
18. Rek V, Němec I (2016) Parallel computation on multicore processors using explicit form of the finite element method and C++ standard libraries. J Mech Eng 66(2):67–78. https://doi.org/10.1515/scjme-2016-0020
19. Li Y, Brossier R, Métivier L (2020) 3D frequency-domain elastic wave modeling with the spectral element method using a massively parallel direct solver. Geophysics 85(2):T71–T88. https://doi.org/10.1190/geo2019-0172.1
20. Zhang J, Ankit A, Gravenkamp H, Eisenträger S, Song C (2021) A massively parallel explicit solver for elasto-dynamic problems exploiting octree meshes. Comput Methods Appl Mech Eng 380:113811. https://doi.org/10.1016/j.cma.2021.113811
21. Goutaudier D, Berthe L, Chinesta F (2021) Proper Generalized Decomposition with time adaptive space separation for transient wave propagation problems in separable domains. Comput Methods Appl Mech Eng 380:113755. https://doi.org/10.1016/j.cma.2021.113755
22. Chinesta F, Ammar A, Cueto E (2010) Recent advances and new challenges in the use of the proper generalized decomposition for solving multidimensional models. Arch Comput Methods Eng 17:327–350. https://doi.org/10.1007/s11831-010-9049-y
23. Quaranta G, Bognet B, Ibañez R, Tramecon A, Haug E, Chinesta F (2018) A new hybrid explicit/implicit in-plane-out-of-plane separated representation for the solution of dynamic problems defined in plate-like domains. Comput Struct 210:135–144. https://doi.org/10.1016/j.compstruc.2018.05.001
24. Ghnatios C, Cueto E, Falco A, Duval J.-L, Chinesta F Spurious-free interpolations for non-intrusive PGD-based parametric solutions: application to composites forming processes. Int J Mater Form. https://doi.org/10.1007/s12289-020-01561-0
25. Clayton R, Engquist B (1977) Absorbing boundary conditions for acoustic and elastic wave equations. Bull Seismol Soc Am 67:1529–1540
26. Gallego-Juarez J Ultrasonic evaluation of elastic properties of directional fiber reinforced composites, Alippi A, Mayer WG (eds) Ultrasonic methods in evaluation of inhomogeneous materials. NATO ASI Series (E: Applied Sciences) 126. https://doi.org/10.1007/978-94-009-3575-4_20
27. Basu U (2009) Explicit finite element perfectly matched layer for transient three-dimensional elastic waves. Int J Numer Meth Engng 77:151–176. https://doi.org/10.1002/nme.2397
28. Semblat J-F, Gandomzadeh A (2011) A simple multi-directional absorbing layer method to simulate elastic wave propagation in unbounded domains. Int J Numer Meth Engng 85:1543–1563. https://doi.org/10.1002/nme.3035
29. Bécache E, Fauqueux S, Joly P (2003) Stability of perfectly matched layer, group velocities and anisotropic waves. J Comput Phys 188(2):399–433. https://doi.org/10.1016/S0021-9991(03)00184-0
30. Li S, Brun M, Djeran-Maigre I, Kuznetsov S (2019) Hybrid asynchronous absorbing layers based on Kosloff damping for seismic wave propagation in unbounded domains. Comput Geotech 109:69–81. https://doi.org/10.1016/j.compgeo.2019.01.019
31. Bathe K Finite element procedures, second edition, 4th printing, Watertown, MA
32. Bognet B, Bordeu F, Chinesta F, Leygue A, Poitou A (2012) Advanced simulation of models defined in plate geometries: 3D solutions with 2D computational complexity. Comput Methods Appl Mech Eng 201–204:1–12. https://doi.org/10.1016/j.cma.2011.08.025
33. Ladevèze P (2014) PGD in linear and nonlinear computational solid mechanics. Separated representations and PGD-based model reduction, Springer, pp 91–152. https://doi.org/10.1007/978-3-7091-1794-1_3
34. Shirafkan N, Bamer F, Stoffel M, Markert B (2020) Quasistatic analysis of elastoplastic structures by the proper generalized decomposition in a space-time approach. Mech Res Commun, p 103500. https://doi.org/10.1016/j.mechrescom.2020.103500
35. Boucinha L, Gravouil A, Ammar A (2013) Space-time proper generalized decomposition for the resolution of transient elastodynamic models. Comput Methods Appl Mech Engrg 255:67–88. https://doi.org/10.1016/j.cma.2012.11.003
36. Boucinha L, Ammar A, Gravouil A, Nouy A (2014) Ideal minimal residual-based proper generalized decomposition for non-symmetric multi-field models—application to transient elastodynamics in space-time domain. Comput Methods Appl Mech Engrg 273:56–76. https://doi.org/10.1016/j.cma.2014.01.019
37. Achenbach J Wave propagation in elastic solids, Elsevier, North Holland
38. Willberg C, Duczek S, Vivar Perez J, Schmicker D, Gabbert U (2012) Comparison of different higher order finite element schemes for the simulation of Lamb waves. Comput Methods Appl Mech Eng 241-244:246–261. https://doi.org/10.1016/j.cma.2012.06.011
39. Duczek S, Gravenkamp H (2019) Mass lumping techniques in the spectral element method: on the equivalence of the row-sum, nodal quadrature, and diagonal scaling methods. Comput Methods Appl Mech Eng 353:516–569. https://doi.org/10.1016/j.cma.2019.05.016
40. Wu S (2006) Lumped mass matrix in explicit finite element method for transient dynamics of elasticity. Comput Methods Appl Mech Eng 195(44):5983–5994. https://doi.org/10.1016/j.cma.2005.10.008
41. Ampuero J. P SEM2DPACK: A spectral element method tool for 2D wave propagation and earthquake source dynamics user's guide, version 2.3.8. https://github.com/jpampuero/sem2dpack
42. Tschöke K, Gravenkamp H (2018) On the numerical convergence and performance of different spatial discretization techniques for transient elastodynamic wave propagation problems. Wave Motion 82:62–85. https://doi.org/10.1016/j.wavemoti.2018.07.002
43. Johnson L (1974) Green's function for Lamb's problem. Geophys J R ASFR Soc 37:99–131
44. Bamberger A, Joly P, Roberts J (1990) Second-order absorbing boundary conditions for the wave equation: a solution for the corner

problem. SIAM J Numer Anal 27(2):323–352. https://doi.org/10.1137/0727021
45. Zhang K, Tang W, Wenhui F, Fu K Modeling of dynamic behavior of carbon fiber-reinforced polymer (CFRP) composite under X-ray radiation, Materials 11. https://doi.org/10.3390/ma11010143